



# Kinematic study of Iquique 2014 $M_w$ 8.1 earthquake: Understanding the segmentation of the seismogenic zone

Jorge Jara<sup>a,\*</sup>, Hugo Sánchez-Reyes<sup>a</sup>, Anne Socquet<sup>a</sup>, Fabrice Cotton<sup>b,c</sup>, Jean Virieux<sup>a</sup>, Andrei Maksymowicz<sup>d</sup>, John Díaz-Mojica<sup>e</sup>, Andrea Walpersdorf<sup>a</sup>, Javier Ruiz<sup>c</sup>, Nathalie Cotte<sup>a</sup>, Edmundo Norabuena<sup>f</sup>

<sup>a</sup> Univ. Grenoble Alpes, Univ. Savoie Mont Blanc, CNRS, IRD, IFSTTAR, ISTerre, F-38000 Grenoble, France

<sup>b</sup> German Research Centre for Geosciences, GFZ Helmholtz Centre Potsdam, Potsdam, Germany

<sup>c</sup> Institute for Earth and Environmental Sciences, University of Potsdam, Potsdam, Germany

<sup>d</sup> Departamento de Geofísica, Facultad de Ciencias Físicas y Matemáticas, Universidad de Chile, Santiago, Chile

<sup>e</sup> Instituto de Geofísica, Universidad Nacional Autónoma de México, México, Mexico

<sup>f</sup> Instituto Geofísico del Perú, Lima, Peru

## ARTICLE INFO

### Article history:

Received 28 February 2018

Received in revised form 15 September 2018

Accepted 19 September 2018

Available online 4 October 2018

Editor: J.P. Avouac

### Keywords:

high-rate GPS  
strong Motion  
megathrust earthquakes  
kinematic inversion  
subduction segmentation

## ABSTRACT

We study the rupture processes of Iquique earthquake  $M_w$  8.1 (2014/04/01) and its largest aftershock  $M_w$  7.7 (2014/04/03) that ruptured the North Chile subduction zone. High-rate Global Positioning System (GPS) recordings and strong motion data are used to reconstruct the evolution of the slip amplitude, rise time and rupture time of both earthquakes. A two-step inversion scheme is assumed, by first building prior models for both earthquakes from the inversion of the estimated static displacements and then, kinematic inversions in the frequency domain are carried out taken into account this prior information. The preferred model for the mainshock exhibits a seismic moment of  $1.73 \times 10^{21}$  Nm ( $M_w$  8.1) and maximum slip of  $\sim 9$  m, while the aftershock model has a seismic moment of  $3.88 \times 10^{20}$  ( $M_w$  7.7) and a maximum slip of  $\sim 3$  m. For both earthquakes, the final slip distributions show two asperities (a shallow one and a deep one) separated by an area with significant slip deficit. This suggests a segmentation along-dip which might be related to a change of the dipping angle of the subducting slab inferred from gravimetric data. Along-strike, the areas where the seismic ruptures stopped seem to be well correlated with geological features observed from geophysical information (high-resolution bathymetry, gravimetry and coupling maps) that are representative of the long-term segmentation of the subduction margin. Considering the spatially limited portions that were broken by these two earthquakes, our results support the idea that the seismic gap is not filled yet.

© 2018 Elsevier B.V. All rights reserved.

## 1. Introduction

On 1 April 2014, a  $M_w$  8.1 subduction earthquake struck the North of Chile offshore Iquique. This earthquake is of interest for two main reasons. First, the megathrust rupture was preceded by a long precursory phase characterized by a slow slip event that lasted several months (Kato et al., 2016; Socquet et al., 2017), and interactions between shallow and intermediate-depth seismicities (Bouchon et al., 2016; Jara et al., 2017) that ended into an intense foreshock sequence, which origin remains debated in terms

of slip behavior (Ruiz et al., 2014; Meng et al., 2015; Kato et al., 2016). This precursory phase has been the focus of many studies, while the present paper targets another interesting questions raised by Iquique earthquake. The mainshock occurred in a mature seismic gap, where a moment deficit equivalent to  $\sim M$  8.6 has been accumulating since the 1877 historical earthquake (e.g., Métois et al., 2016) (Fig. 1). With a moment magnitude  $M_w$  8.1, Iquique earthquake was therefore significantly smaller than what could be feared in this area, and the different published slip models show that the earthquake together with its largest aftershock of  $M_w$  7.7 broke a spatially limited area ( $\sim 200$  km along the subduction) (e.g., Hayes et al., 2014; Lay et al., 2014; Ruiz et al., 2014; Duputel et al., 2015; Liu et al., 2015), leaving two regions with the potential capability to generate earthquakes of  $M_w \geq 8.0$  (Hayes et al., 2014; Ruiz et al., 2014; Duputel et al., 2015). However, the reason why this earthquake together with its largest aftershock broke

\* Corresponding author.

E-mail address: jara@geologie.ens.fr (J. Jara).

<sup>1</sup> Now at Laboratoire de Géologie, Département de Géosciences, ENS, CNRS, UMR8538, PSL Research University, Paris, France.

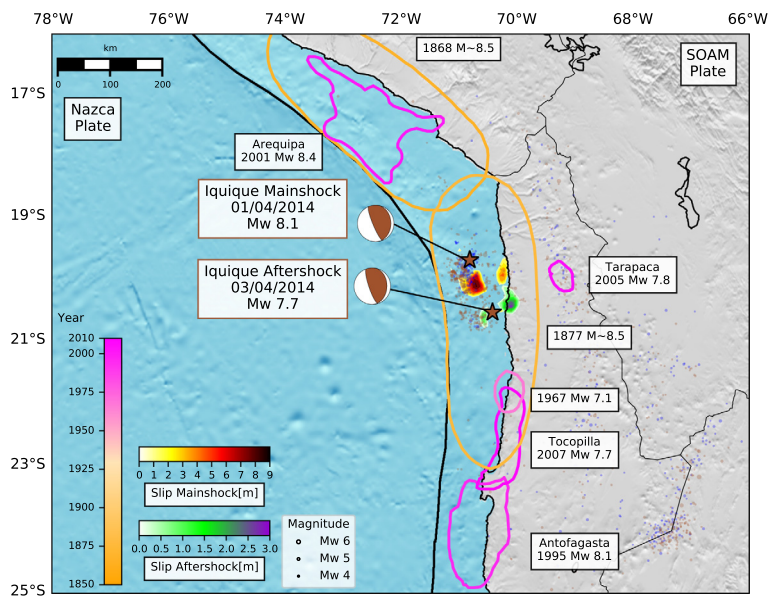


**Fig. 1.** (a) Seismotectonic Context of North Chile–South Peru subduction zone. Historical and instrumental rupture areas are color coded as a function of their date of occurrence. Dates and magnitudes of all earthquakes  $M > 7.0$  in the area are indicated in squared boxes. Mainshock ( $M_w$  8.1 2014/04/01) and aftershock ( $M_w$  7.7 2014/04/03) focal mechanisms from Duputel et al. (2015) are color coded by time. Stars symbolize the mainshock and aftershock epicenters from CSN catalog, as well as the seismicity since 2013/07/01 up to 2014/12/31 with magnitudes over 4.0, color coded by time (blue dots denote events before the mainshock and dark brown events after it) and scaled by magnitude. Preferred slip models for the mainshock and aftershock are plotted with colors depending on the slip. (For interpretation of the colors in the figure(s), the reader is referred to the web version of this article.)

only this specific limited portion of the seismic gap remains elusive. What are the physical conditions (slip deficit, state of stress, friction or structural complexity) that contributed to enhance the ruptures, to end it? Do these earthquakes contribute to fill the slip deficit derived from interseismic geodetic coupling? Are the mechanisms that trigger the mainshock similar to the ones that initiate the aftershock? Is the ruptured area structurally peculiar? Here we explore these questions by studying the rupture process of the Iquique earthquake and its biggest aftershock ( $M_w$  7.7, 2014/04/03), and then by comparing our results with complementary geophysical data that describe the interseismic coupling and the structural complexity in the area.

This earthquake has been well recorded by geodetic and strong motion networks (including co-located stations), providing a unique opportunity to explore the compatibility of both datasets and to show how high-rate GPS can help to better constrain the kinematic rupture processes. We perform a two-step inversion in the frequency domain proposed by Hernandez et al. (1999), that consists in carrying out a static inversion, used as prior information in the kinematic models to explore the source of both earthquakes. Inverting in the frequency domain presents the advantage of evaluating how each frequency is explained (or not) by the inverted slip model. This approach offers the opportunity to have a continuum (in the frequency domain) between the static and kinematic solution. However, frequency domain inversions have not been improving so much these last years and there is then a need to take into account the recent development and ideas of the slip inversion community (multigrad analysis (Bunks et al., 1995), sensitivity analysis (Duputel et al., 2015), better control of the smoothing process (Wellington et al., 2017)), that are explored during this work.

## 2. Data analysis

### 2.1. High-rate continuous GPS

High-rate GPS (HRGPS, 1 Hz) data from different networks located in South Peru–North Chile (IPOC, LIA “Montessus de Ballore”, CAnTO, ISTERre, IGP and CSN, Fig. S1) are processed using TRACK

software (Herring et al., 2016). We use the LC combination and IGS precise orbits, employing the atmospheric delay estimated from daily GPS processing each 2 hours (see Supplementary Material for further details). TRACK computes a relative position with respect to a reference station supposed to be fixed. Here, we have chosen as a reference UCNF station (Fig. S1), located  $\sim 150$  km from the epicenters. When the seismic waves reach the reference station, its movement is reflected in the computed displacements of the whole network. This effect, together with orbital errors, is corrected by removing a common mode from the original signal and a sidereal filtering is applied to dismiss the multipath effects (Figs. S2 and S3). The static coseismic offsets are then estimated by fitting a step function in the HRGPS signal, 500 s before and after the earthquake (Fig. S4 and Table S1).

### 2.2. Strong motion versus HRGPS seismograms

Strong motion stations located in North Chile from different networks are employed in this study (IPOC, LIA “Montessus de Ballore” and CSN, Figs. 4 and 6b). The signals are twice integrated to obtain the ground displacements, and then filtered between 0.01–0.5 Hz. These signals are compared to those from collocated HRGPS. HRGPS signals are filtered in the same frequency band as strong-motion ones. The superposition of both signals shows an excellent consistency in waveform (Fig. S5). This procedure confirms the relevance of using HRGPS for the kinematic inversion of displacements, avoiding the double integration procedure of the strong motion data which induces some uncertain amplifications.

## 3. Static and kinematic inversion procedures

Let us first consider procedures for this two-step inversion where both the spatial discretization and the model covariance matrices play crucial roles for reducing the intrinsic ill-posedness of this inversion problem. To deal with this problem and because we do not apply any slip positivity constrain (thus allowing larger slip variability), we have imposed several regularization schemes as explained below.

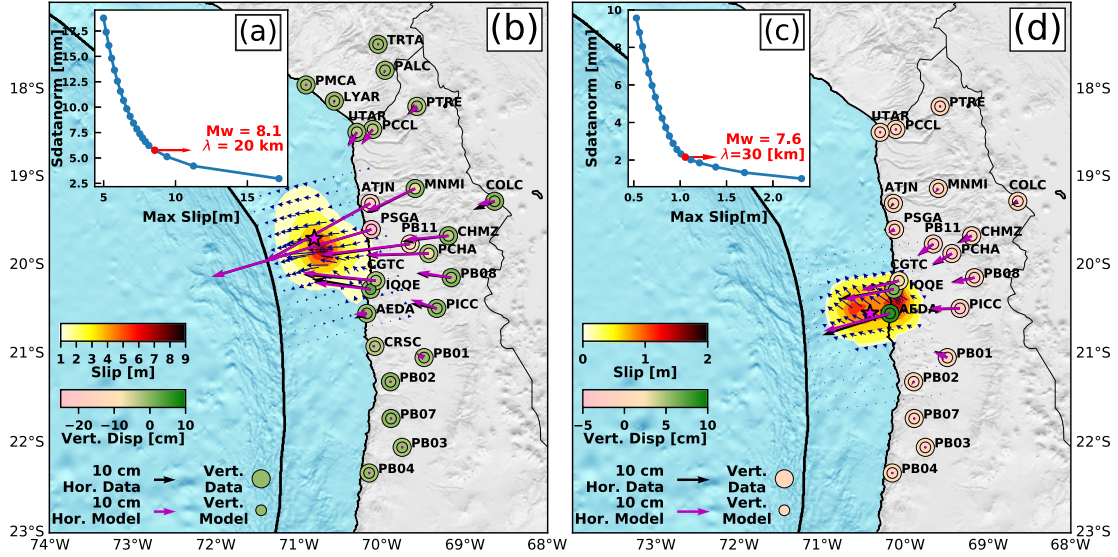


**Fig. 2.** Static inversion results obtained using HRGPS for the mainshock and the aftershock. (a), (c) Normalized misfit as a function of the maximum slip, showing the correlation length of the preferred slip model for mainshock ((a)  $\lambda = 20$  km) and aftershock ((c)  $\lambda = 30$  km). Slip model and comparison between data and model (horizontal in arrows and vertical in circles) for the mainshock (b) and aftershock (d). Pink stars symbolize the epicenter of the events reported by the CSN catalog. The dark blue arrows denote the slip direction for both earthquakes, scaled by the slip amplitude.

### 3.1. Static inversion

GPS static displacements are inverted for the mainshock ( $M_w$  8.1, 2014/04/01, Fig. 2b) and for the biggest aftershock ( $M_w$  7.7, 2014/04/03, Fig. 2d) to get the final slip distribution associated with both earthquakes. A fault of 210 km  $\times$  175 km is discretized into 12 subfaults of 17.5 km along-strike and 14 subfaults of 12.5 km along-dip. The dip of the fault progressively increases with depth (the shallower segment dips at 5°, followed by a segment at 9°, 3 segments at 15°, 4 at 20° and finally the 5 deepest segments at 23°). A constant strike is considered (346° for the mainshock and 352° for the aftershock). The rake angle is allowed to vary within the two perpendicular directions to the convergence angle of N77°E. In both cases, the fault plane is fixed to a geometry compatible with the one of Slab 1.0 (Hayes et al., 2012) (Fig. S6). The static Green's functions are calculated through the discrete-wave-number method (Bouchon, 1981) in an elastic stratified medium with AXITRA program (Coutant, 1989), employing the velocity model proposed by Peyrat et al. (2010) (Table S2). This procedure allows us to calculate the complete Green's functions, therefore the static displacement is given by the zero-frequency, expressed as a linear function of the static slip through the expression  $Gm$ .

For each station, the three components of the displacement field, compactly designed as  $d$ , are inverted altogether in a least-squares sense (Tarantola, 2005), where the misfit function  $S$  is defined as:

$$S(m) = \frac{1}{2} [(Gm - d)^t C_d^{-1} (Gm - d) + (m - m_0)^t C_m^{-1} (m - m_0)], \quad (1)$$

where the data and the model covariances are noted respectively  $C_d$  and  $C_m$ , and  $m_0$  is the initial or prior model. The expected slip model  $m$  is defined by:

$$m = m_0 + C_m G^t (G C_m G^t + C_d)^{-1} (d - Gm), \quad (2)$$

where the prior model  $m_0$  is defined as zero static slip for both events. Data covariance matrix  $C_d$  is assumed to contain only diagonal terms with variances ( $\sigma_d^2$ ) associated with estimated errors during the coseismic offsets calculation (Table S1). The model covariance matrix  $C_m$  is going to play an important role in building the slip, requiring a band-diagonal structure given by

$$C_m(\mathbf{x}, \mathbf{x}') = \left( \frac{\lambda_0}{\lambda_{dip} \lambda_{strike}} \right) \sigma(\mathbf{x}) \mathcal{F}(\mathbf{x}, \mathbf{x}'), \quad (3)$$

where the scaling factor  $\lambda_0$  is usually taken as the size of an individual subfault (Radiguet et al., 2011) (here 15 km for both events). This band-limited structure of the covariance matrix reduces its model-square complexity down to a more manageable model-like complexity. The model correlation between two different positions  $\mathbf{x} = (dip, strike)$  and  $\mathbf{x}' = (dip', strike')$  on the fault plane is expressed by the operator  $\mathcal{F}$ . Its expression with a laplacian decay

$$\mathcal{F}(\mathbf{x}, \mathbf{x}') = \exp \left( - \frac{|dip - dip'|}{\lambda_{dip}} - \frac{|strike - strike'|}{\lambda_{strike}} \right), \quad (4)$$

will provide more coupling than the often used Gaussian decay (Wellington et al., 2017): a key point for mitigating trade-off between parameter values for this static reconstruction. For static inversion, this relatively slow decay behavior has been found to behave better than the often used Gaussian decay (Radiguet et al., 2011). The correlation lengths  $\lambda_{dip}$  and  $\lambda_{strike}$  are considered as homogeneous in this work, although they can be tuned to vary with the fault position, especially when fault points are moving away from acquisition network. Correlation length  $\lambda_{dip}$  has been tested between 5–100 km, with a step each 5 km. Following the L-curve criterion (Hansen, 1992), we have chosen the best compromise between the maximum slip and the normalized misfit (Fig. 2 a and c): optimal values are 20 km (mainshock) and 30 km (aftershock).

The operator  $\sigma(x)$  (with a model complexity) expresses the prior expected local variability or sensitivity of the static slip: small values will prevent the static slip reconstruction to move away from the prior model value which is zero in our case. The operator  $\sigma(x)$  compensates for poor geometry of the acquisition with respect to the active fault. The lack of sensitivity with depth can also be controlled by this operator. Moreover, we may increase the sensitivity of zones where we expect high values when fitting the data. The following operator

$$\sigma(x) = \sigma_{min} + (\sigma_{max} - \sigma_{min}) \times \exp \left( - \frac{|dip - dip_0|}{\lambda_{dip_0}} - \frac{|strike - strike_0|}{\lambda_{strike_0}} \right) \quad (5)$$



has been selected where the position ( $dip_0, strike_0$ ) is the zone with the most expected variation of the static slip for the mainshock. We have assumed a circular shape through the choice for quantities  $\lambda_{dip_0}$  and  $\lambda_{strike_0}$  equal to 40 km and 40 km respectively, with values ranging from 0.01 to 2.5 m. For the aftershock, such single-shape operator has been considered in a first trial: the data gradient still drives us toward two zones of maximum slip. Therefore, we have considered in a second trial two joint prior shapes with  $\sigma$  values ranging from 0.01 to 1.0 m around these expected high-slip zones: the data gradient has built up a solution coherent with this second sensitivity design. In both cases  $\lambda_{dip_0}$  and  $\lambda_{strike_0}$  are equal to 25 km and 52.5 km.

For the final solution, the model resolution is evaluated following the resolution matrix proposed by Tarantola and Valette (1982), given by

$$R = C_m G^t (G C_m G^t + C_d)^{-1} G, \quad (6)$$

gives us low resolution for all subfaults (Fig. S7 for mainshock and Fig. S8 for the aftershock, a and b): for a perfectly resolved model, the matrix should be the identity. On the other hand, the data sensitivity defined by Duputel et al. (2015) through

$$Sen = diag(G^t C_d^{-1} G) \quad (7)$$

shows the ability of the network to detect slip at a given location on the fault (Fig. S7 for mainshock and Fig. S8 for the aftershock, c and d).

### 3.2. Kinematic inversion

The kinematic reconstruction of the rupture process is an even more ill-posed problem because of possible leakages between space and time: we have followed the two-step strategy proposed by Hernandez et al. (1999) for a reconstruction in the frequency domain building the solution by sweeping from low to high frequencies. At each frequency, the static solution obtained from inversion of geodetic data will be used as the prior model in the kinematic inversion. The synthetic displacement waveform in the frequency domain is computed following the sparse parameterization proposed by Cotton and Campillo (1995), given by

$$V_i(w) = \sum_{k=1}^n G_{ski}(w) [slip_{sk} \exp(-iwt_k) S_k(R_k, w)] + \sum_{k=1}^n G_{dki}(w) [slip_{dk} \exp(-iwt_k) S_k(R_k, w)], \quad (8)$$

where the Green's function (i.e. the displacement for a unit constant slip on the  $k$ -th subfault for the frequency  $w$ ) is denoted by the symbol  $G_{ski}$  for the strike component and by  $G_{dki}$  for the dip. The slip is parametrized depending on the component as well: slip along-strike by  $slip_{sk}$  and slip along-dip by  $slip_{dk}$ . The rupture time is indicated by  $t_k$ , while the source time function (STF) is given by the following analytical expression  $S_k(t) = 0.5(1 + \tanh(t + R_k/2.0)^2)$ , depending on the rise time  $R_k$ . Therefore, only four parameters have to be reconstructed for each subfault. Each subfault is represented by an array of point sources, separated by distances of less than one sixth of the shortest wavelength to be considered locally. For these point sources, Green's functions are computed and then, the sum of all point sources response delayed in time to include the travel-time difference, due to the rupture front propagation across each subfault (Cotton and Campillo, 1995). The Green's functions are calculated using the same strategy as for the static inversion with the program AXITRA (Coutant, 1989), but keeping the whole frequency range. We do

not consider variable rupture velocity inside each subfault which is allowed to slip once. The velocity model is the same as the one used during the static inversion for both events.

The four parameters, namely strike slip, dip slip, rise time and rupture time in each subfault, are inverted using the non-linear least-squares formulation proposed by Tarantola and Valette (1982). A non-linear operator  $f$  relates the model parameters  $m$  to the data vector  $d$  through the general expression  $d = f(m)$ . The model solution is obtained through an repetitive procedure based on a linearized approximation where the next model  $m_{l+1}$  is obtained from the current model  $m_l$  following the iterative algorithm

$$m_{l+1} = m_l + b(A_l^t C_d^{-1} A_l + C_m^{-1})^{-1} \times (A_l^t C_d^{-1} (d - f(m_l)) + C_m^{-1} (m_0 - m_l)), \quad (9)$$

which minimizes the least-squares data misfit. At each frequency, the initial model  $m_0$  will be used also as a prior model. For the lowest frequency, the static solution will be considered as the initial/prior model and the final solution at this frequency will be used as the initial/prior model for the next frequency. The Jacobian matrix  $A_l$  are obtained by taking the closed-form derivative of the Equation (8) with respect to the related parameter. The damping factor  $b$  between 0 and 1 prevents any divergence. The data covariance  $C_d$  has a diagonal matrix filled with ones, for simplicity considering the stations' spatial distribution, while the model covariance requires more attention as we see in the multigrid approach we associate with the frequency sweeping.

Based on a multigrid approach, the inversion starts with a Large Subfault Size (LSS) discretization sweeping over frequencies, obtaining a final solution (Bunks et al., 1995). The final solution is interpolated in a Small Subfault Size (SSS) discretization, repeating again the inversion scheme with another set of frequency windows still sweeping from low to high frequencies. By combining this dynamic frequency sampling and a recursive spatial sampling, we are able to improve the data fit and to increase the model resolution with still stable results. For the LSS sampling, we have adopted the same subfault geometry employed during the static inversion (168 subfaults). The SSS sampling is obtained by dividing each subfault in four subsequent subfaults, so that the total fault encompasses 672 subfaults (24 along-strike with 8.75 km and 28 along-dip with 6.25 km) for both events.

The inversion procedure is performed by using a progressively broadened frequency range for both events for fixed spatial sampling. The LSS model is initiated with a frequency range of 0.01–0.02 Hz using the static solution as the initial/prior model. The obtained solution is then used as the new initial/prior model for the new frequency range of 0.01–0.03 Hz. This procedure is repeated until the frequency range of 0.01–0.25 Hz is reached (24 models in total). The last LSS model is then interpolated and used as the initial/prior model for the SSS sampling, considering the first frequency range of 0.01–0.02 Hz. The same iterative procedure is repeated for the small-subfaults configuration until the frequency range of 0.01–0.3 Hz is reached (29 models in total).

For both events, the model covariance matrix  $C_m$  is defined as a matrix, following Radiguet et al. (2011). The variances  $\sigma_{strike}$  and  $\sigma_{dip}$  are defined following the Equation (5) with the same strategy employed during the static inversion. The  $\sigma_{rup\_time}$  is defined with the same idea as in Equation (5), but increasing the values from the epicenter of the earthquakes, because the rupture time may be better estimated near the epicenter, but not far from it. We have started by allowing a considerable variability through  $\sigma_{dip}$  (main slip direction) and  $\sigma_{rup\_time}$ , but a lower one in the strike slip component (Table S3). When the seismic moment reported for the earthquakes is reached, we keep the same proportion mentioned to define  $\sigma$  in terms of variability, but reducing the values

between which parameters are allowed to move, in order to hold the seismic moment (Table S3). There is no physical reason to constrain the rise time, so we have assigned the same  $\sigma_{rise\_time}$  value to all subfaults in both models and events (LSS and SSS, Table S3).

In order to avoid spurious jumps in the model parameters (slip along-dip and strike, rise time), we introduce a correlation length of 17.5 km in LSS model and 8.75 km in SSS model, for both events. It allows to connect the adjacent subfaults providing a smooth rupture process. To evaluate the fit to the data, we compute the variance reduction proposed by Cohee and Beroza (1994). The sensitivity is also analyzed (Equation (7)) for the mainshock (Fig. S15) and the aftershock (Fig. S16).

## 4. Results

### 4.1. Static inversion

The mainshock (Fig. 2a) has broken an asperity localized between 15–40 km depth with a maximum slip of  $\sim 9$  m. It is located South of the epicenter reported by CSN ( $\sim 40$  km). The seismic moment obtained is  $1.52 \times 10^{21}$  Nm, equivalent to  $M_w$  8.1. The dominant slip direction is on the dip-slip component, observing some strike-slip component at the south-east of the rupture plane. The aftershock (Fig. 2b) is composed of two asperities localized on each side of the epicenter, with a maximum slip of  $\sim 1.2$  m. The shallower asperity (close to the trench) is confined between 15–30 km depth, and the deeper one between 40–50 km depth. The seismic moment obtained from the inversion is  $3.68 \times 10^{20}$  Nm, associated with an earthquake magnitude  $M_w$  7.6. The main dominant slip direction is in the north-west component, which is not the convergence direction. We find as an interesting point the fact the slip vectors of the aftershock point towards the mainshock asperity. Our hypothesis is that this feature might be related to the stress generated by the mainshock, producing a particular behavior of the slip vectors (increasing the amount of its strike-slip component). Comparing those slip models to the resolution analysis (resolution matrix and sensitivity), we find that the data can better resolve the slip close to the coast than close to the trench (Fig. S7 for the mainshock and Fig. S8 for the aftershock). The poor resolution obtained at the trench vicinity is typical for subduction zones lacking offshore instrumentation, due to the lack of data close to the trench. The results are good enough to be used as our prior model in the kinematic inversion, especially because the spatial distribution is well resolved where the slip is located.

### 4.2. Kinematic inversion

#### 4.2.1. Mainshock

Some differences can be appreciated between the resulting kinematic and static slip distributions. The final slip obtained during the kinematic inversion shows a very concentrated asperity South of the epicenter ( $\sim 43$  km) with a maximum slip of  $\sim 9$  m and confined between 15–35 km depth. Conversely to the static solution, less slip is seen North of the epicenter and the emergence of a second deep asperity is observed between 40 and 55 km depths (Fig. 3a) with a maximum slip of 5 m. The main slip direction is on the dip-slip component.

The rupture is characterized by a very slow moment rate during the first 25 s, leading to an abrupt acceleration at the moment liberation at 30 s (Fig. 3 e and f). After that, the moment rate decreases to reach the final rupture time at 125 s (Fig. 3 e and f). The total seismic moment obtained is  $1.73 \times 10^{21}$  Nm (Fig. 3e), equivalent to a magnitude  $M_w$  8.1 and a stress drop of 7.8 MPa. The difference between data and synthetics corresponds to a mean variance reduction of 82.37% (see Table 1), fitting better the lower

**Table 1**

Mainshock and Aftershock moment estimations and data fit using different parameterizations.

No of subfaults	Starting rup. front vel. (km/s)	Moment $\times 10^{21}$ (Nm)	Mean variance reduction (%)
<b>Mainshock</b>			
168	1.2	1.92	76.65
168	1.3	1.74	78.53
168	1.4	1.71	79.73
168	1.5	1.62	79.15
168	1.6	1.57	79.20
168	1.7	1.52	77.71
672	1.4	1.73	82.37
<b>Aftershock</b>			
168	2.4	0.423	81.56
168	2.5	0.428	81.75
168	2.6	0.404	83.26
168	2.7	0.430	82.15
168	2.8	0.432	81.96
672	2.6	0.388	85.74

frequencies 0.01–0.15 Hz (Fig. 3d). At higher frequencies, a limited variance reduction up to 0.2 Hz is obtained. This is also visible in the data fit, where the low frequencies are better fitted (Fig. 4a, see Supplementary Information for not normalized and frequency domain fit, Figs. S11 and S13), while the high frequencies are not well solved. Some complexity in the rupture time (Fig. 3b) and rise time (Fig. 3c) are required to the South of the rupture to fit the signal of Southern stations. This complexity is also reflected in the STF after the 75 s (Fig. 3f). To the North, the rupture propagates at a much more constant rate than to the South (Fig. 3b). This variation in complexity might be associated with changes in the lithology that are not reflected in the velocity model. To evaluate the kinematic solution in terms of the static model, a forward static model is performed (Fig. S17a). A large misfit is found for stations ATJN and PSGA indicating that a significant portion of slip is missed by the kinematic inversion in the northern part of the rupture. Interestingly, this amount of slip that is missed by the kinematic inversion is located in an area where the rise time is high and rupture time is rather slow compared to the main peaks of slip, which may explain a tiny signal in the accelerometer data that mostly cover this portion of the rupture. To solve this inconsistency, we have performed another static inversion of coseismic displacements keeping the same values for lambda and data covariance matrix as those described in section 3.1, but using the final kinematic slip distribution as prior model and constant covariance matrix defined as 10% of the maximum slip. This is meant to test whether it is possible to obtain static solution that remains close to our kinematic model (Fig. 7 and Fig. S17c). It allows us to improve the solution of static displacements, holding the slip features that appeared during the kinematic inversion and fitting well the measured coseismic offsets. We have performed the same procedure for the aftershock case (Fig. 7b and Fig. S17d), although there is not a big discrepancy between the final kinematic slip model and the static displacements obtained during the forward mode (Fig. S17b).

#### 4.2.2. Aftershock

The slip distribution of the largest aftershock is characterized by two asperities located on both sides of the epicenter (Fig. 5a). The shallow asperity is confined between 15–30 km depths with a maximum slip of 1.5 m, while the deeper one is located between 30–50 km depths with a maximum slip of  $\sim 3$  m (Fig. 5a, see Supplementary Information for not normalized and frequency domain fit, Figs. S12 and S14). The calculated seismic moment is  $3.88 \times 10^{20}$  Nm, equivalent to a magnitude  $M_w$  7.7 (Fig. 5 e and f) and a stress drop of 1.8 MPa. The main slip direction for the

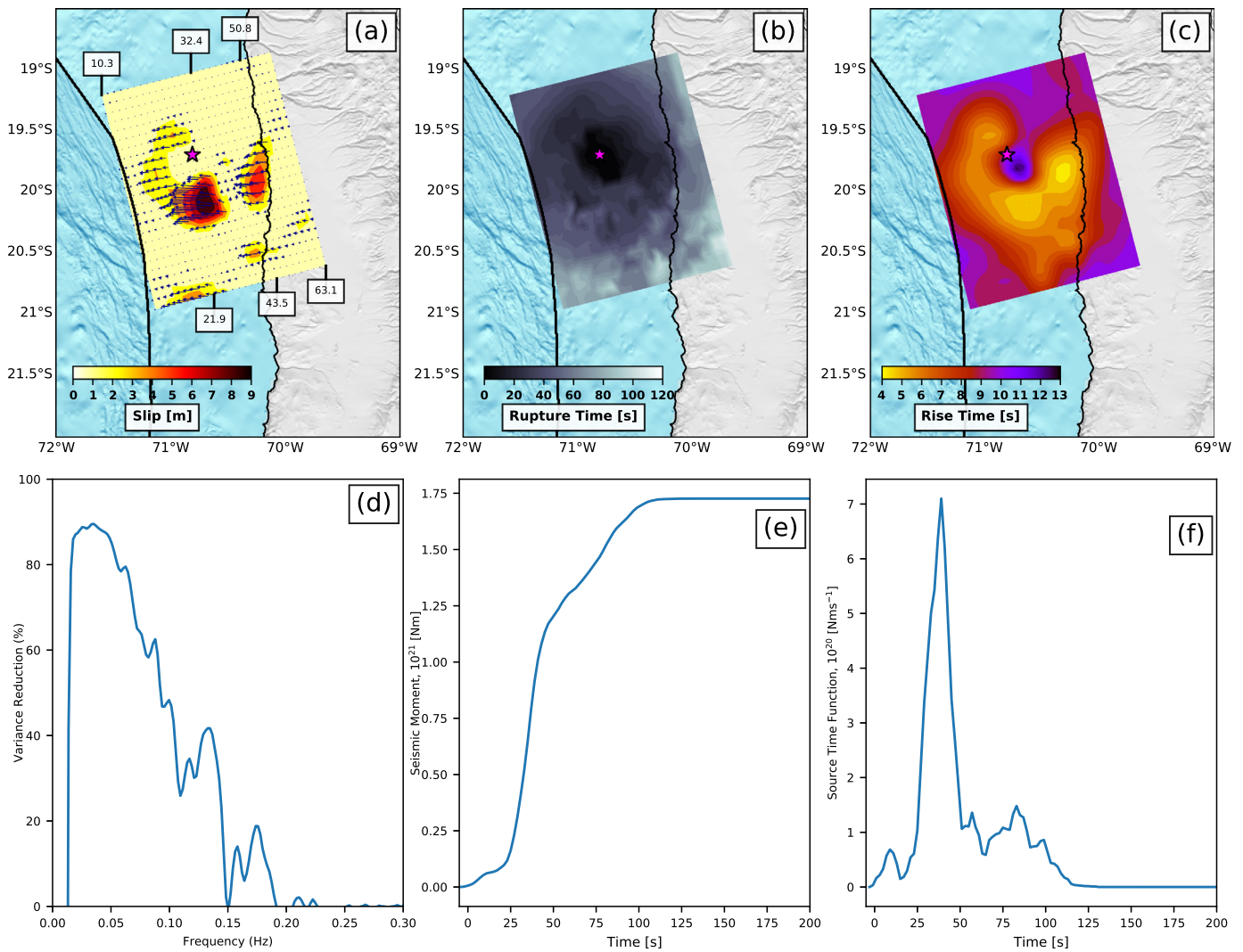


**Fig. 3.** Mainshock kinematic inversion results. Preferred slip model (a), rupture time (b) and rise time (c). Plane depths are indicated inside white boxes in (a). The pink star indicates the epicenter location reported by CSN catalog and the dark blue arrows denote the slip direction, scaled by the slip amplitude. (d) Mean variance reduction computed for each frequency between data of all the stations and synthetics. (e) Cumulative seismic moment and (f) STF.

shallower asperity is on the dip-slip component, while the deeper one is oriented in the north-west component. The result obtained during the kinematic inversion is similar to the static one, but provides further details in the asperities location and the slip distribution.

The rupture has begun with an acceleration during the first 18 s (Fig. 5e), breaking the asperity close to the trench. Then, the second deeper asperity has slipped during 20 s (Fig. 5e). The STF is simpler than the mainshock (Fig. 5f), and lasts 60 s. The fit to the data corresponds to a mean variance reduction of 85.74%, solving the frequency range of 0.01–0.3 Hz (Fig. 5d). Although not significant differences are found in the static forward model obtained using the final kinematic slip model (Fig. S17b), we have repeated the strategy described above to obtain the final aftershock static model (Fig. 7b).

#### 4.2.3. Comparison between LSS and SSS models

LSS and SSS models have been compared in order to explore the differences and advantage of SSS model for the mainshock (Fig. S9) and the aftershock (Fig. S10). For both earthquakes, the spatial resolution of the model discretization is increased. Rupture time (Figs. S9 and S10c, d) and rise time (Figs. S9 and S10e, f) show the same variation as the slip, but do not change the general pictures of their behaviors are not changed, thanks to the multigrad

approach. One important change between LSS and SSS models is the increase in the frequency range resolution. For the mainshock (Fig. S9g), the resolution is improved by about 40% in the frequency range of 0.1–0.15 Hz. At higher frequencies, the resolution still slightly increases ( $\sim 15\%$ ), but not significantly. For the aftershock (Fig. S10, g) the SSS models improves significantly the mean variance reduction in the frequency range 0.1–0.25 Hz. The seismic moment obtained with both models is of the same order (Figs. S9 and S10h, i). The STF show some differences between LSS and SSS models (Figs. S9 and S10i): the STF is slightly more smoothed in the SSS models due to the change in the subfault size, avoiding any large change of the parameters between the adjacent subfaults. The resolution of the kinematic models (Figs. S15 for the mainshock and S16 for the aftershock) is similar between LSS and SSS models.

The number of parameters inverted during the inversion increases from 672 in the LSS model to 2688 parameters in the SSS model. For both earthquakes the model resolution close to the trench is quite low because the stations are located inland. The increase of the number of parameters seems to reduce the local resolution on each subfault, but the spatial pattern of the resolution is kept (well resolved close to the epicenter, and poorly resolved by the trench, Figs. S15 and S16).



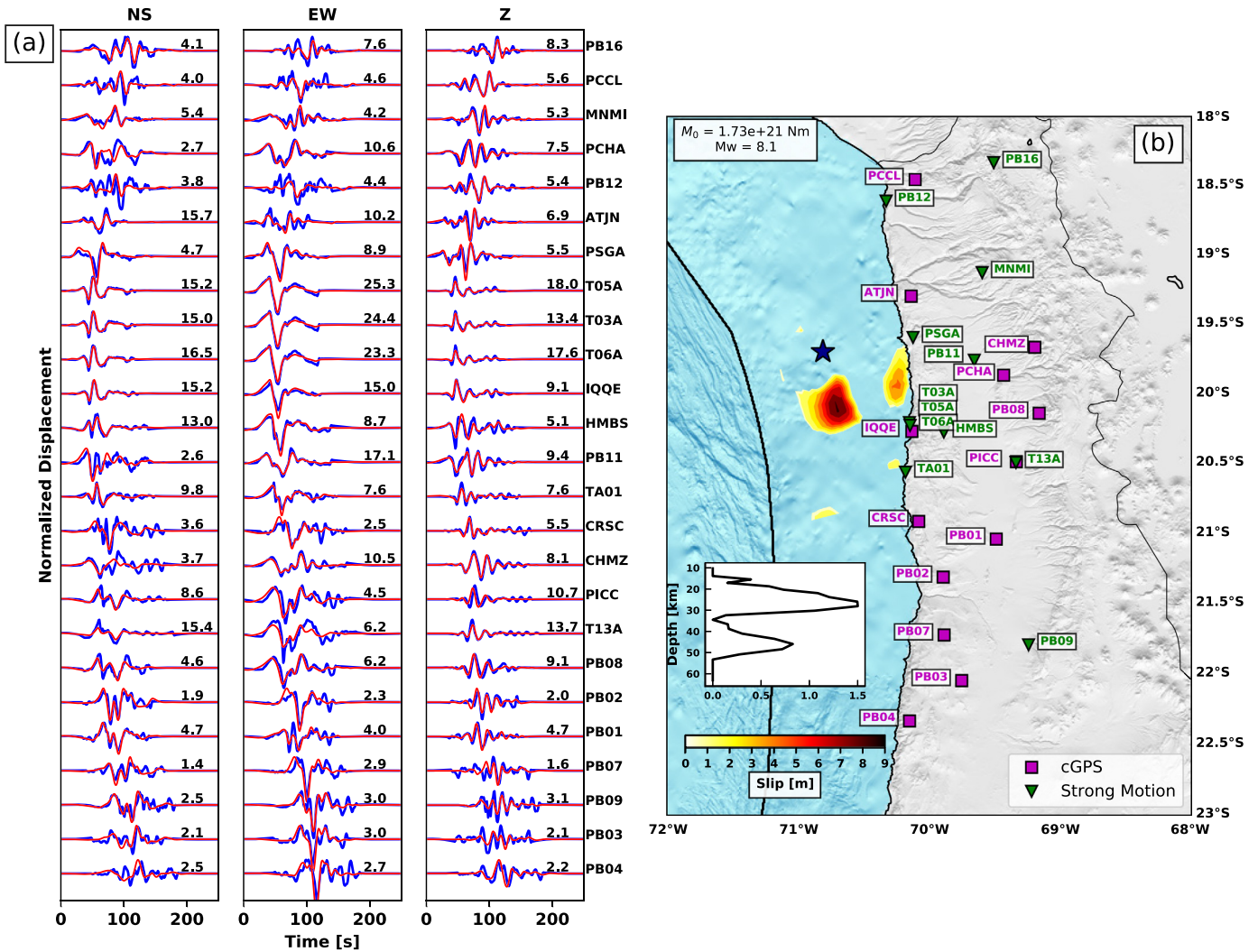


**Fig. 4.** (a) Mainshock normalized Strong Motion – HRGPS (blue) and synthetic seismograms (red). For each station and component, the maximum data displacement is shown in [cm]. (b) Final preferred slip model and stations map used during the kinematic inversion. Green triangles symbolize strong motion location and magenta squares HRGPS. Star indicates the epicenter of the event by CSN catalog. Also, at the bottom left is shown the slip averaged along-strike as a function of depth.

**5. Discussion**

**5.1. Along-strike segmentation of the seismogenic zone**

Our results confirm that 2014  $M_w$  8.1 Iquique earthquake together with its largest aftershock ruptured a limited portion of the seismic gap (Fig. 1). Moreover, the obtained slip distributions show that both earthquakes ruptured into two distinct asperities, quite spatially concentrated (Fig. 8).

Following Aki (1979), it is therefore likely that the earthquake stopped because it encountered a geometric or inhomogeneous barrier. It has been proposed that large earthquakes rupture areas that are strongly coupled, while aseismic slip is seen in poorly coupled zones and it has been proposed to act as a barrier for seismic ruptures. This might be supported by the occurrence of preseismic slow slip surrounding the main slip patches of the mainshock (Socquet et al., 2017) (Fig. 9d). Our coseismic slip distribution compared to the interseismic slip distribution obtained by Métois et al. (2016) tends to confirm this finding, at least for the mainshock (Fig. 9c). The mainshock was initiated in an area at the transition between low and high coupling, prone to high stresses, possibly even further loaded by the 8-month slow slip that preceded the rupture. The earthquake has then propagated Southward and ruptured a highly locked patch, and eventually stopped at the

Southern termination of this highly coupled patch (Fig. 9c). The mainshock has therefore contributed to release the slip deficit accumulated in this locked asperity during the interseismic period.

On the contrary, the largest aftershock has broken areas that were poorly coupled in the interseismic period (Fig. 9c). In order to understand this apparent contradiction, we have calculated the stress change produced by the mainshock on the subduction plane (Fig. 8a). The aftershock is located in areas with positive Coulomb Stress change (Fig. 8a), suggesting that it has been triggered by the mainshock stress increase. Fig. 8a shows towards the north of the epicenter, the CSC is more heterogeneous than the southern region. Towards the north, the slab is changing the strike because of the Arica bend, which is not represented in our geometry employed in the inversion procedures (dip variable and strike constant on the fault plane). It might explain the positives values of the CSC in the northern region not observing large aftershocks. Also, Fig. 9 (c and d) shows the region struck by the mainshock is surrounded by preseismic slip. The region where the aftershock is emplaced is the only place where not coseismic slip is observed, that combined with the positives values of the CSC, it might explain the triggering of this event by the mainshock.

To further understand the parameters that control the location of such a seismic asperity and high coupling patch, we compared our findings with the bathymetry and the free-air gravity anomaly

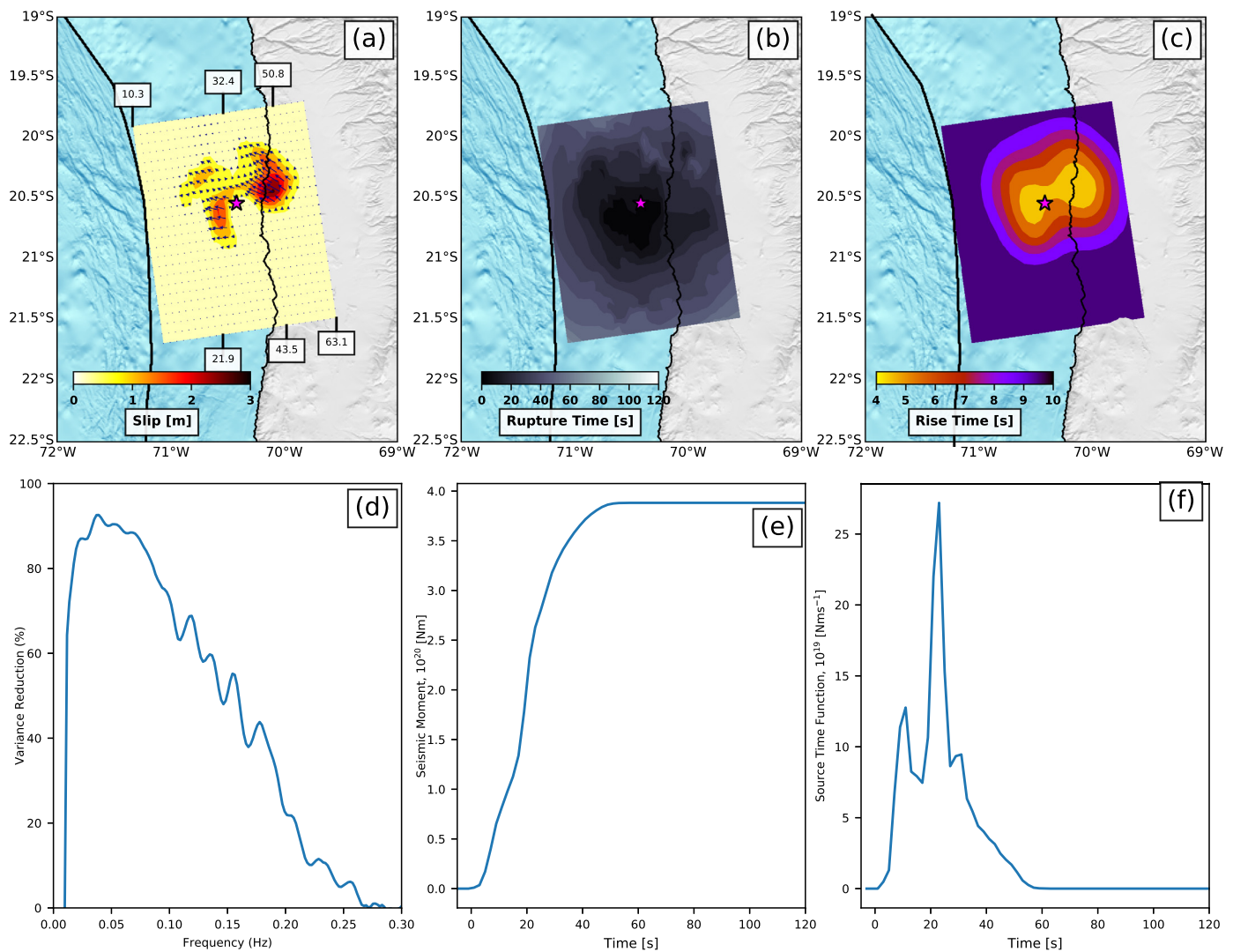


Fig. 5. Same caption as in Fig. 3, but for the aftershock case.

(Fig. 9 a and b). Geological features affecting the subducting slab or the overriding plate (such as fracture zones, ridges, changes in the slab geometry, peninsulas, fault systems and marine basins) have been shown to correlate with low coupling zones and the arrest of seismic rupture (e.g., Armijo and Thiele, 1990; Song and Simons, 2003; Wells et al., 2003; Audin et al., 2008; Béjar-Pizarro et al., 2010; Contreras-Reyes et al., 2012; Maksymowicz et al., 2015), and can be interpreted as a structural complexity that acts as a geometrical barrier for the seismic rupture (Aki, 1979; King, 1986). Using seismic velocity profiles and gravity data, Wells et al. (2003) evidenced a spatial correlation between forearc basins and the peak of slip of several great earthquakes, suggesting that the basin is an indicator of a long-term seismic moment release. Song and Simons (2003) have proposed another way to analyse the gravity data through the definition of the Trench Parallel Gravity Anomaly (TPGA), where areas of negative values correlate with the coseismic slip in subduction zones.

The asperity with highest slip value of 2014 Iquique mainshock is centered in the Iquique basin (Armijo et al., 2015), inferred from high resolution bathymetry (Fig. 9a) and free-air gravity anomaly (Fig. 9b). This is in agreement with the results shown and discussed by Meng et al. (2015), who demonstrated that the main asperity is located in an area with negative value of TPGA. The Southern limit of the main rupture is characterized by an important change in the gravity reported by Maksymowicz et al. (2018),

who have modeled the free-air anomaly (Fig. 9b) and the local gravity data in the northern Chile region. Probably, this feature is associated with a change in the lithology, fracturing and fluid content inside the continental wedge. Considering that tectonic erosion is characteristic along the Northern Chile margin, the distance between the deformation front and the shelf break increases in the northern segment of the study area and the lower slope decreases. This feature suggests the presence of a wider frontal sedimentary prism to the north, and in general, a latitudinal tectonic segmentation of the continental wedge, which is supported by velocity models (Comte et al., 2016) and density gravity models (Maksymowicz et al., 2018). This strong gravity change is associated with a geological change that could explain the complexity observed in the Southern part of the rupture and the heterogeneities in the tail of the STF (Fig. 3b and f).

The North limit of the aftershock also seems related to the gravity changes discussed above. This sharp change marks an E–W line that separates both earthquakes. The Southern limit of the aftershock is not associated with any clear change in the gravity, but might be related to geological features of the overriding plates responsible to stop the rupture. Audin et al. (2008) have pointed out the relationship between the Chololo coastal fault system and the Southern end of Arequipa coseismic rupture in Peru ( $M_w$  8.4, 2001, Fig. 1). The tectonic map of González et al. (2003) indicates that the region where the aftershock stops at 21°S is characterized by



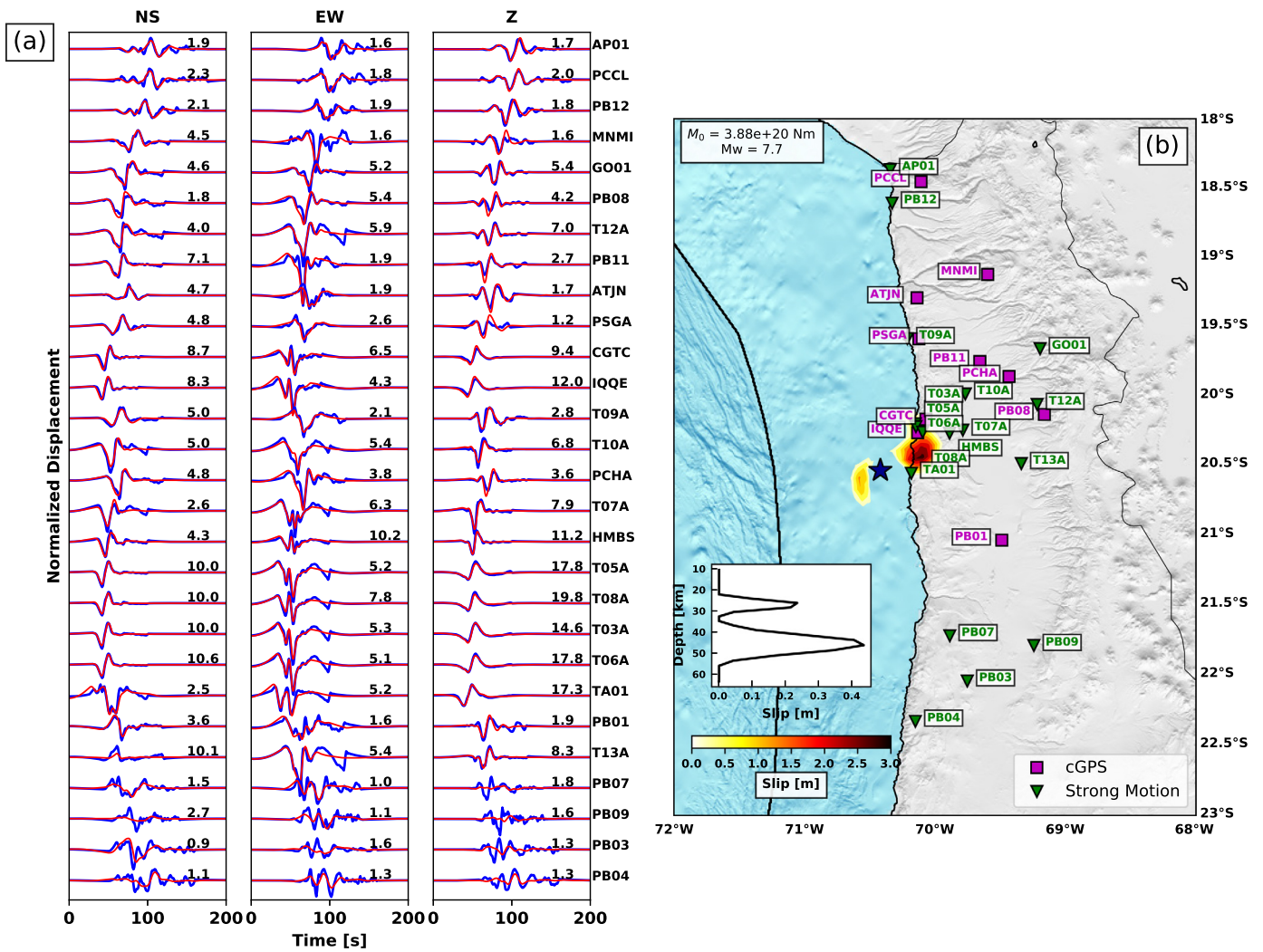


Fig. 6. Same caption as in Fig. 4, but for the aftershock case.

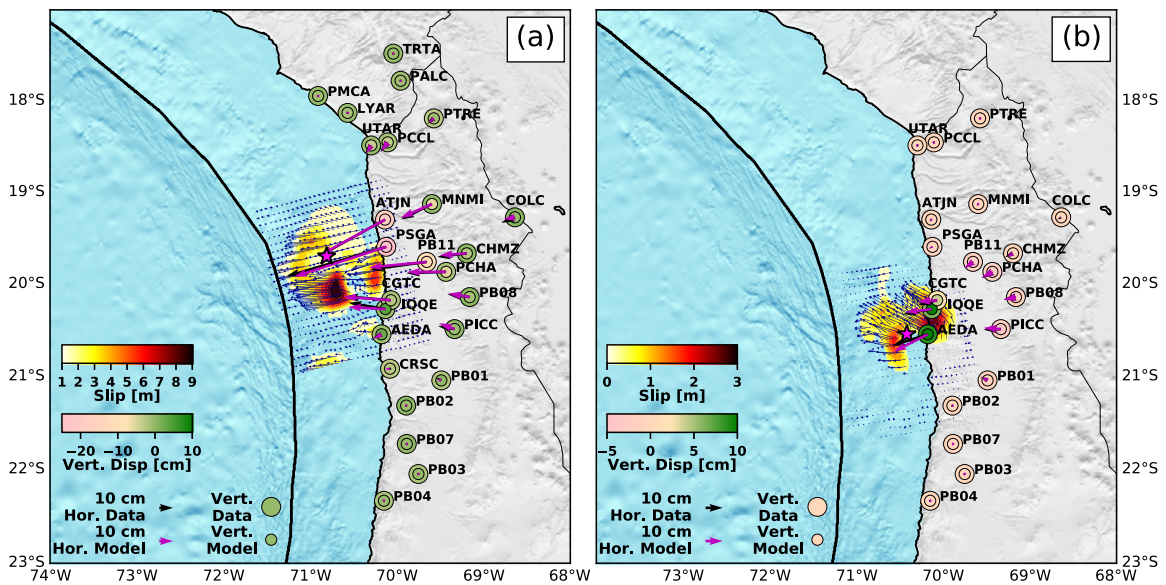
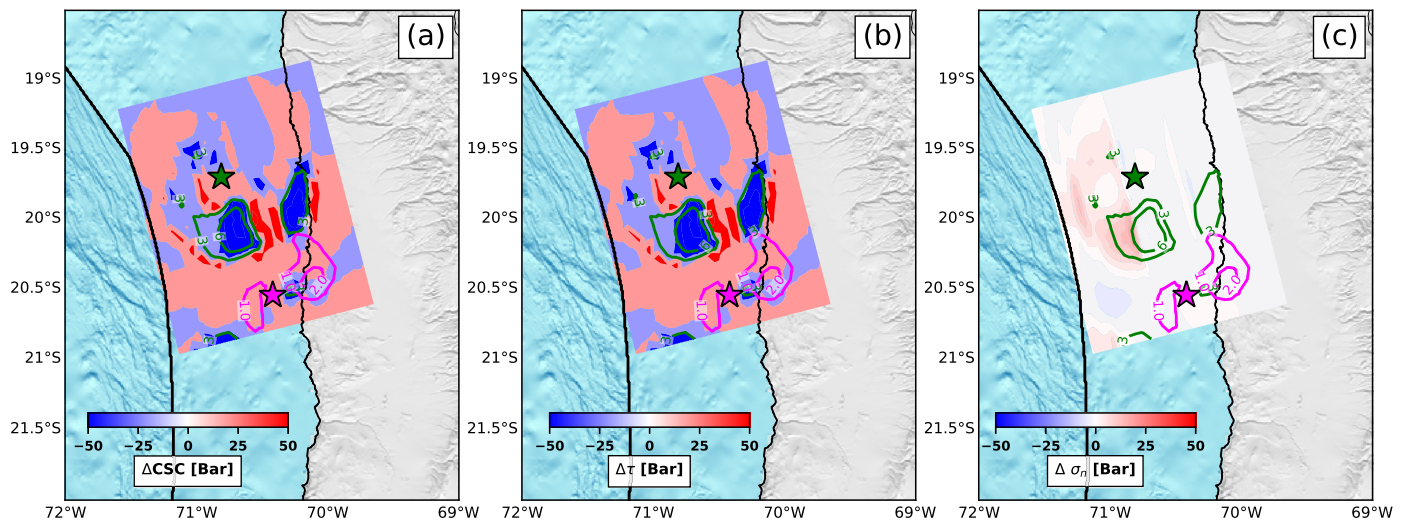


Fig. 7. (a) Mainshock (b) Aftershock) static inversion results obtained using the kinematic slip model as the prior model. A small value for the model covariance ( $C_m$ ) is used to perform the inversion (10% of the maximum slip for each event). Slip model and comparison between data and model (horizontal in arrows and vertical in circles) are plotted and color coded. Pink stars symbolize the epicenter of the events reported by the CSN catalog. The dark blue arrows denote the slip direction for both earthquakes, scaled by the slip amplitude.



**Fig. 8.** Coulomb stress change (a), shear stress change (b) and normal stress change (c) on the fault plane calculated using the mainshock preferred slip model. Green (pink) star and contours denote the epicenter of the mainshock (aftershock) reported by CSN catalog and the slip produced by the event (see Supplementary Material for further information about the calculation).

an increased complexity in the faults system. South of 21°S almost all the faults are parallel to the trench and the coastal scarp (mainly normal faults), but North to this limit, the area of the Salar Grande is affected by a series of E–W thrust faults combined with conjugated strike-slip faults (González et al., 2003). This tectonic difference might be related to the Southern termination of the aftershock rupture.

### 5.2. Along-dip segmentation of the seismogenic zone

Both the mainshock and the large aftershock show an interesting bimodal pattern along-dip (Fig. 4b and Fig. 6b). In both cases, the shallow patch of slip extends from 15 km and 30 km depths, while the deep patch of slip is confined between 35 and 50 km depths. The upper limit at 15 km depth corresponds to the deformation front extracted from gravity (Maksymowicz et al., 2018) and seismic velocity models (Comte et al., 2016). The downdip limit at ~50 km depth is in agreement with other seismological (Comte and Suárez, 1995) and geodetic (Béjar-Pizarro et al., 2010; Chlieh et al., 2011; Métois et al., 2016) definitions of the lower extent of the seismogenic zone in North Chile subduction.

The most intriguing aspect of the observed along-dip segmentation is the separation between shallow and deep asperities. Indeed both earthquakes present almost no slip at 30–35 km depths. Armijo and Thiele (1990) proposed that the coastal scarp could be a west-dipping normal fault reaching the subduction zone at depth. A change in the slab dip has been inferred from wide-angle seismic refraction and reflection data, complemented with relocated aftershock seismicity in the Tocopilla area (~22°S) (Contreras-Reyes et al., 2012) ( $M_w$  7.7, 2007, Fig. 1). Based on a correlation with the coastal scarp and following the idea proposed by Armijo and Thiele (1990), the authors suggest that this change in dip from 10° to 22° affects a wide portion of the slab. Maksymowicz et al. (2018) have modeled the gravimetry in the region observing the same change in dip proposed by Contreras-Reyes et al. (2012) in the Tocopilla area. Employing those results, we have inferred the location towards the North of this change in the dip (purple line in Fig. 9 a and b), observing that in the area affected by Iquique earthquake, this feature seems to delimit a separation between the deep and shallow asperities. This change in slab geometry may therefore act as a barrier for the rupture by slowing its velocity and reducing the amount of slip between the shallow and deep asperities. Such an along-dip segmentation had already

been observed in the area during the 2007 Tocopilla earthquake that ruptured the deeper part of the seismogenic interface (Béjar-Pizarro et al., 2010).

This along-dip segmentation is also associated with a change in the frequency content of the seismic rupture. The deeper asperities both rupture into a pulse of slip that is much shorter than the slippage of the shallower asperities (as shown from the rise time and the rupture time, Fig. 3 b and c and Fig. 5 b and c). Meng et al. (2015) and Lay et al. (2014) have shown a compatible observation: back-projected high-frequency energy is radiated in the deeper portion of the rupture, close to deep asperity. Although the structural complexity might be invoked, numerical simulations also provide the simple explanation that the base of the coupled area is a zone of high prestress that tends to keep partial ruptures confined, producing pulse-like ruptures that propagate along-strike (Michel et al., 2017). Such observations are compatible with the along-dip segmentation of the megathrust described in North Chile from the analysis of the frequency content of moderate magnitude earthquakes (Piña-Valdés et al., 2018). Also, Lay (2015) characterizes the segmentation of the subduction zone through four domains (A, B, C and D), based on the radiated energy generated by the earthquakes, using teleseismic data. Domain A corresponds to depths less than 15 km, experiencing either aseismic deformation or large coseismic displacement in tsunami earthquakes. Domain B is located between 15 and 35 km, observing the nucleation of megathrust earthquakes that generate large slip and high amount of low-frequency radiation. Domain C is localized between 35–60 km depths, where a large amount of high-frequency radiation is emitted and asperities much smaller than region B are seen. Finally, the Domain D is placed deeper than 60 km and is where slow slip events, low-frequency events, and seismic tremor have been reported, and it is not reported in all subduction zones. Following the model proposed by Lay (2015), our results show that the shallow asperities for the mainshock such as the aftershock, are located at depths between 15 and 35 km, suggesting they would break the Domain B. Also, for both events, the deeper asperities are emplaced at depths between 35 and 60 km, suggesting they would break the Domain C, depicting the heterogeneity of the seismogenic zone. This segmentation along dip in terms of frequency content during the earthquake ruptures has been already reported in Chile. After the Maule earthquake ( $M_w$  8.8, 2010), Kiser and Ishii (2011) and Wang and Mori (2011) show that high-frequency radiation is predominant in the deeper part of the



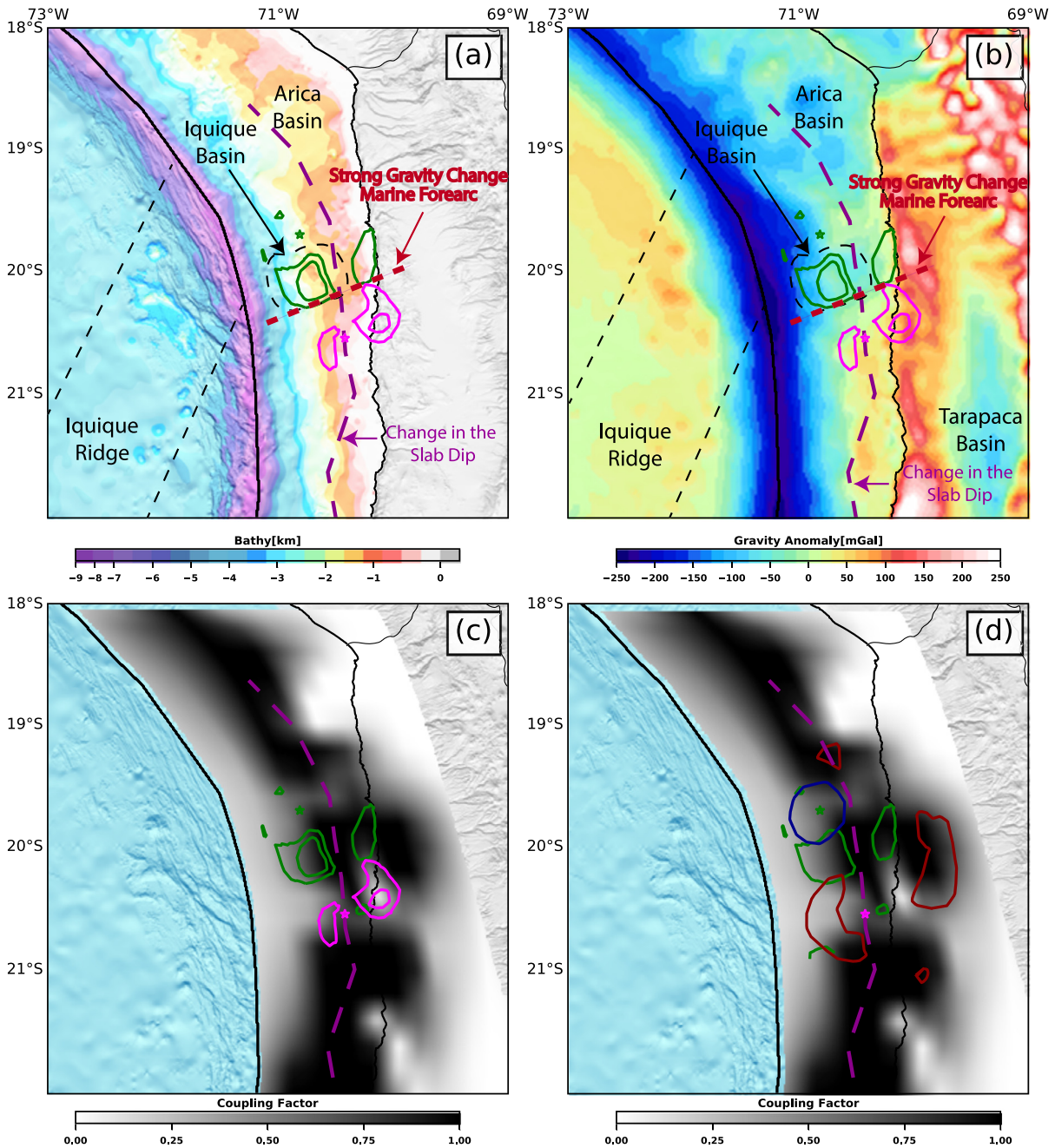


**Fig. 9.** (a) High-resolution topography (Contreras-Reyes et al., 2012), (b) free air gravity anomaly (Sandwell et al., 2014) and (c) and (d) coupling distribution (Métouis et al., 2016) on the study area. Mainshock (green) and aftershock (pink) slip contour of 2.0 m and 0.5 m are plotted. Violet line parallel to the trench represents the abrupt change on dip proposed by Contreras-Reyes et al. (2012) interpolated to the North, extracted from gravity models. (d) Coupling map with the mainshock contours (green), the 8-month SSE (red) and the 2-week preseismic slip (dark blue) shown by Socquet et al. (2017) contoured in mm.

seismogenic zone. Similar results have been observed after the occurrence of Illapel earthquake ( $M_w$  8.4, 2015) (Melgar et al., 2016; Ruiz et al., 2016).

### 5.3. Differences between our results and previous works

Our results are very consistent with those presented by Duputel et al. (2015) for the mainshock as well for the aftershock, although we use a different methodology. The main difference between their work and ours is the emergence of a previously unnoticed deep slip asperity. Our initial static slip model is not able to see this feature, because GPS data are poorly sensitive to deep slip (see for instance the predicted displacement generated by the deep asperity only as dark blue arrows in Fig. S17a). Also, it seems this

deep feature is resolved by waveforms of frequencies over 0.05 Hz (Fig. S18). In the kinematic result, this deep slip is needed to fit the maximum amplitude of displacement, notably at the closest stations that are less well fit by Duputel et al. (2015) or Liu et al. (2015) (Fig. S19). Another difference between their work and ours, is the number of stations used in near-field range for the kinematic inversion. We have employed 25 HRGPS and strong motion while they have used 19 HRGPS and strong motion (plus all the other data set). We have found a rupture with 125 s of duration, they have used just 80 s. This longer rupture allows us to observe the second deep asperity and the complexity of the rupture process to the South. We have found a similar static patch as Duputel et al. (2015) for the aftershock, but our results are clearer because we



have included more data. Comparing our mainshock results with those of Liu et al. (2015), we obtain the same shallow asperity, but their slip is closer to the trench and further North with respect to the epicenter. The difference in the obtained slip can be attributed to the simpler geometry used by Liu et al. (2015) that does not follow a realistic slab geometry. We conclude that the parametrization of the fault plane is a first-order characteristic input required to perform kinematics inversions. For both events, we have used more near-field data than Liu et al. (2015), allowing to get a better resolution and the apparition of the second deep asperity. The use of HRGPS therefore seems to improve the resolution of the rupture process, filling the data gap in areas where strong motion instruments are not installed.

When authors have used teleseismic data to invert the rupture process (Lay et al., 2014; Hayes et al., 2014), the differences are due to the lack of resolution of those datasets to resolve details that the near-field data can distinguish, although obtaining similar values for the seismic moment, maximum slip and mean stress drop (e.g., Lay et al., 2014; Hayes et al., 2014; Ye et al., 2016; Hayes, 2017). Also, our models present more details in terms of the rupture process than the static inversions (e.g., Socquet et al., 2017) because modeling the waveforms provides details occurring during the rupture that a static change cannot see. The results obtained by Meng et al. (2015) seem to move all asperities landward, using repetitive earthquakes and backprojection. As they do not have any prior information of where the asperities provided by the static inversion or teleseismic data are located, we suspect that their results are affected by a shift in the asperity localization, providing a general picture about the slip, but incrementing the resolution in terms of the frequency content generation through back-projection technique.

## 6. Conclusions

The kinematic rupture process of Iquique earthquake  $M_w$  8.1 and its biggest aftershock  $M_w$  7.7 provides interesting insights about the segmentation of the seismogenic zone. Both ruptures are confined within 15–50 km depths, with a low slip zone that separates shallow and deep asperities, which may be related to a change of dip in the subducting slab (or bending of it). We show that the segmentation along-strike depends on several factors. The mainshock is centered on a forearc basin associated with an important gravity change in the area of  $\sim 20.5^\circ\text{S}$ , limiting the rupture to the South. The aftershock rupture might have stopped in the vicinity of a fault system dissecting the overriding plate. Several aseismic processes may affect the rupture extension, including the long precursory slow slip surrounding the mainshock area, and the spatial distribution of interseismic coupling before the earthquake. The mainshock contributed to fill the slip deficit in the area, but changed the stresses in the region and likely triggered the biggest aftershock that ruptured a poorly coupled zone. An along-dip segmentation is also observed, notably in the frequency content of the earthquakes, in agreement with previous works in the area (Meng et al., 2015; Piña-Valdés et al., 2018). These results are very important in the perspective of the seismic hazard studies, where the segmentation is a primordial element of the models.

## Acknowledgements

The authors thank the International Plate Boundary Observatory Chile (IPOC, [www.ipoc-network.org](http://www.ipoc-network.org)), Laboratoire International Associé “Montessus de Ballore” ([www.lia-mb.net](http://www.lia-mb.net)), Central Andean Tectonic Observatory Geodetic Array (CAnTO, [http://www.tectonics.caltech.edu/resources/continuous\\_gps.html](http://www.tectonics.caltech.edu/resources/continuous_gps.html)), Instituto Geofísico del Perú ([www.igp.gob.pe](http://www.igp.gob.pe)) and Centro Sismológico Nacional de Chile (CSN, [www.csn.uchile.cl](http://www.csn.uchile.cl)) for making the raw GPS

and strong motion data available. Jorge Jara acknowledges a Ph.D. scholarship granted by Chilean National Science Cooperation (CONICYT) through “Becas Chile” Program. Hugo Sanchez-Reyes thanks the Centre National de la Recherche Scientifique (CNRS) for a Ph.D. scholarship. This work has been supported by grants from Labex OSUG@2020 (Investissement d’avenir – ANR10 LAB56), IRD AO-Sud, and by ANR-17-CE31-0002-01 AtypicSSE. This work was partially supported by funding from the European Research Council (ERC) under the European Union’s Horizon 2020 research and innovation program (grant agreement 758210, project Geo4D). The authors would like to thank E. Contreras-Reyes, M. Radiguet, M. Causse, L. Audin, J. Pina-Valdes, R. Jolivet, H. Bhat, C. Vigny and M. Bouchon for all the constructive discussions about this work. Finally, the authors thank Z. Duputel, an anonymous reviewer, and the Editor J.P. Avouac for their constructive comments.

## Appendix A. Supplementary material

Supplementary material related to this article can be found online at <https://doi.org/10.1016/j.epsl.2018.09.025>.

## References

- Aki, K., 1979. Characterization of barriers on an earthquake fault. *J. Geophys. Res., Solid Earth* 84 (B11), 6140–6148.
- Armijo, R., Lacassin, R., Coudurier-Curveur, A., Carrizo, D., 2015. Coupled tectonic evolution of Andean orogeny and global climate. *Earth-Sci. Rev.* 143, 1–35.
- Armijo, R., Thiele, R., 1990. Active faulting in Northern Chile: ramp stacking and lateral decoupling along a subduction plate boundary? *Earth Planet. Sci. Lett.* 98 (1), 40–61.
- Audin, L., Lacan, P., Tavera, H., Bondoux, F., 2008. Upper plate deformation and seismic barrier in front of Nazca subduction zone: the Chololo fault system and active tectonics along the coastal Cordillera, Southern Peru. *Tectonophysics* 459 (1), 174–185.
- Béjar-Pizarro, M., Carrizo, D., Socquet, A., Armijo, R., Barrientos, S., Bondoux, F., Bonvalot, S., Campos, J., Comte, D., De Chabaliér, J., et al., 2010. Asperities and barriers on the seismogenic zone in North Chile: state-of-the-art after the 2007  $M_w$  7.7 Tocopilla earthquake inferred by GPS and InSAR data. *Geophys. J. Int.* 183 (1), 390–406.
- Bouchon, M., 1981. A simple method to calculate Green’s functions for elastic layered media. *Bull. Seismol. Soc. Am.* 71 (4), 959–971. <http://www.bssaonline.org/content/71/4/959.abstract>.
- Bouchon, M., Marsan, D., Durand, V., Campillo, M., Perfettini, H., Madariaga, R., Gardonio, B., 2016. Potential slab deformation and plunge prior to the Tohoku, Iquique and Maule earthquakes. *Nat. Geosci.* 9 (5), 380–383.
- Bunks, C., Saleck, F.M., Zaleski, S., Chavent, G., 1995. Multiscale seismic waveform inversion. *Geophysics* 60 (5), 1457–1473.
- Chlieh, M., Perfettini, H., Tavera, H., Avouac, J.-P., Remy, D., Nocquet, J.-M., Rolandone, F., Bondoux, F., Gabalda, G., Bonvalot, S., 2011. Interseismic coupling and seismic potential along the Central Andes subduction zone. *J. Geophys. Res., Solid Earth* 116 (B12).
- Cohee, B.P., Beroza, G.C., 1994. Slip distribution of the 1992 Landers earthquake and its implications for earthquake source mechanics. *Bull. Seismol. Soc. Am.* 84 (3), 692–712.
- Comte, D., Carrizo, D., Roecker, S., Ortega-Culaciati, F., Peyrat, S., 2016. Three-dimensional elastic wave speeds in the Northern Chile subduction zone: variations in hydration in the supraslab mantle. *Geophys. Suppl. Mon. Not. R. Astron. Soc.* 207 (2), 1080–1105.
- Comte, D., Suárez, G., 1995. Stress distribution and geometry of the subducting Nazca plate in Northern Chile using teleseismically recorded earthquakes. *Geophys. J. Int.* 122 (2), 419–440.
- Contreras-Reyes, E., Jara, J., Grevemeyer, I., Ruiz, S., Carrizo, D., 2012. Abrupt change in the dip of the subducting plate beneath North Chile. *Nat. Geosci.* 5 (5), 342–345.
- Cotton, F., Campillo, M., 1995. Frequency domain inversion of strong motions: application to the 1992 Landers earthquake. *J. Geophys. Res., Solid Earth* 100 (B3), 3961–3975.
- Coutant, O., 1989. Program of numerical simulation AXITRA. *Res. Rep. LGIT (in French)*, Université Joseph Fourier, Grenoble.
- Duputel, Z., Jiang, J., Jolivet, R., Simons, M., Rivera, L., Ampuero, J.-P., Riel, B., Owen, S., Moore, A., Samsonov, S., et al., 2015. The Iquique earthquake sequence of April 2014: Bayesian modeling accounting for prediction uncertainty. *Geophys. Res. Lett.* 42 (19), 7949–7957.
- González, G., Cembrano, J., Carrizo, D., Macci, A., Schneider, H., 2003. The link between forearc tectonics and Pliocene–Quaternary deformation of the Coastal Cordillera, Northern Chile. *J. South Am. Earth Sci.* 16 (5), 321–342.

- Hansen, P.C., 1992. Analysis of discrete ill-posed problems by means of the L-curve. *SIAM Rev.* 34 (4), 561–580.
- Hayes, G.P., 2017. The finite, kinematic rupture properties of great-sized earthquakes since 1990. *Earth Planet. Sci. Lett.* 468, 94–100.
- Hayes, G.P., Herman, M.W., Barnhart, W.D., Furlong, K.P., Riquelme, S., Benz, H.M., Bergman, E., Barrientos, S., Earle, P.S., Samsonov, S., 2014. Continuing megathrust earthquake potential in Chile after the 2014 Iquique earthquake. *Nature* 512 (7514), 295–298.
- Hayes, G.P., Wald, D.J., Johnson, R.L., 2012. Slab1.0: a three-dimensional model of global subduction zone geometries. *J. Geophys. Res., Solid Earth* 117 (B1).
- Hernandez, B., Cotton, F., Campillo, M., 1999. Contribution of radar interferometry to a two-step inversion of the kinematic process of the 1992 Landers earthquake. *J. Geophys. Res., Solid Earth* 104 (B6), 13083–13099.
- Herring, T., King, R.W., Floyd, M.A., McClusky, S.C., 2016. GAMIT, Reference Manual. Department of Earth, Atmospheric, and Planetary Sciences, Massachusetts Institute of Technology.
- Jara, J., Socquet, A., Marsan, D., Bouchon, M., 2017. Long-term interactions between intermediate depth and shallow seismicity in North Chile subduction zone. *Geophys. Res. Lett.* 44 (18), 9283–9292. <https://doi.org/10.1002/2017GL075029>.
- Kato, A., Fukuda, J., Kumazawa, T., Nakagawa, S., 2016. Accelerated nucleation of the 2014 Iquique, Chile Mw 8.2 earthquake. *Sci. Rep.* 6.
- King, G., 1986. Speculations on the geometry of the initiation and termination processes of earthquake rupture and its relation to morphology and geological structure. *Pure Appl. Geophys.* 124 (3), 567–585.
- Kiser, E., Ishii, M., 2011. The 2010 Mw 8.8 Chile earthquake: triggering on multiple segments and frequency-dependent rupture behavior. *Geophys. Res. Lett.* 38 (7).
- Lay, T., 2015. The surge of great earthquakes from 2004 to 2014. *Earth Planet. Sci. Lett.* 409, 133–146.
- Lay, T., Yue, H., Brodsky, E.E., An, C., 2014. The 1 April 2014 Iquique, Chile, Mw 8.1 earthquake rupture sequence. *Geophys. Res. Lett.* 41 (11), 3818–3825.
- Liu, C., Zheng, Y., Wang, R., Xiong, X., 2015. Kinematic rupture process of the 2014 Chile Mw 8.1 earthquake constrained by strong-motion, GPS static offsets and teleseismic data. *Geophys. J. Int.* 202 (2), 1137–1145.
- Maksymowicz, A., Ruiz, J., Vera, E., Contreras-Reyes, E., Ruiz, S., Arraigada, C., Bonvalot, S., Bascuñan, S., 2018. Heterogeneous structure of the Northern Chile marine forearc and its implications for megathrust earthquakes. *Geophys. J. Int.* 215 (2), 1080–1097.
- Maksymowicz, A., Tréhu, A.M., Contreras-Reyes, E., Ruiz, S., 2015. Density-depth model of the continental wedge at the maximum slip segment of the Maule Mw 8.8 megathrust earthquake. *Earth Planet. Sci. Lett.* 409, 265–277.
- Melgar, D., Fan, W., Riquelme, S., Geng, J., Liang, C., Fuentes, M., Vargas, G., Allen, R.M., Shearer, P.M., Fielding, E.J., 2016. Slip segmentation and slow rupture to the trench during the 2015, Mw 8.3 Illapel, Chile earthquake. *Geophys. Res. Lett.* 43 (3), 961–966.
- Meng, L., Huang, H., Bürgmann, R., Ampuero, J.P., Strader, A., 2015. Dual megathrust slip behaviors of the 2014 Iquique earthquake sequence. *Earth Planet. Sci. Lett.* 411, 177–187.
- Métois, M., Vigny, C., Socquet, A., 2016. Interseismic coupling, megathrust earthquakes and seismic swarms along the Chilean subduction zone (38°–18°S). *Pure Appl. Geophys.* 173 (5), 1431–1449.
- Michel, S., Avouac, J.-P., Lapusta, N., Jiang, J., 2017. Pulse-like partial ruptures and high-frequency radiation at creeping-locked transition during megathrust earthquakes. *Geophys. Res. Lett.* 44 (16), 8345–8351. <https://doi.org/10.1002/2017GL074725>.
- Peyrat, S., Madariaga, R., Buforn, E., Campos, J., Asch, G., Vilotte, J., 2010. Kinematic rupture process of the 2007 Tocopilla earthquake and its main aftershocks from teleseismic and strong-motion data. *Geophys. J. Int.* 182 (3), 1411–1430.
- Piña-Valdés, J., Socquet, A., Cotton, F., Specht, S., 2018. Spatiotemporal variations of ground motion in Northern Chile before and after the 2014 Mw 8.1 Iquique megathrust event. *Bull. Seismol. Soc. Am.* 108 (2), 801–814.
- Radiguet, M., Cotton, F., Vergnolle, M., Campillo, M., Valette, B., Kostoglodov, V., Cotte, N., 2011. Spatial and temporal evolution of a long term slow slip event: the 2006 Guerrero slow slip event. *Geophys. J. Int.* 184 (2), 816–828.
- Ruiz, S., Klein, E., del Campo, F., Rivera, E., Poli, P., Métois, M., Christophe, V., Baez, J.C., Vargas, G., Leyton, F., et al., 2016. The seismic sequence of the 16 September 2015 Mw 8.3 Illapel, Chile, earthquake. *Seismol. Res. Lett.* 87 (4), 789–799.
- Ruiz, S., Métois, M., Fuenzalida, A., Ruiz, J., Leyton, F., Grandin, R., Vigny, C., Madariaga, R., Campos, J., 2014. Intense foreshocks and a slow slip event preceded the 2014 Iquique Mw 8.1 earthquake. *Science* 345 (6201), 1165–1169.
- Sandwell, D.T., Müller, R.D., Smith, W.H., Garcia, E., Francis, R., 2014. New global marine gravity model from Cryosat-2 and Jason-1 reveals buried tectonic structure. *Science* 346 (6205), 65–67.
- Socquet, A., Valdes, J.P., Jara, J., Cotton, F., Walpersdorf, A., Cotte, N., Specht, S., Ortega-Culaciati, F., Carrizo, D., Norabuena, E., 2017. An 8 month slow slip event triggers progressive nucleation of the 2014 Chile megathrust. *Geophys. Res. Lett.* 44 (9), 4046–4053. <https://doi.org/10.1002/2017GL073023>.
- Song, T.-R.A., Simons, M., 2003. Large trench-parallel gravity variations predict seismic behavior in subduction zones. *Science* 301 (5633), 630–633.
- Tarantola, A., 2005. *Inverse Problem Theory and Methods for Model Parameter Estimation*. SIAM.
- Tarantola, A., Valette, B., 1982. Generalized nonlinear inverse problems solved using the least squares criterion. *Rev. Geophys.* 20 (2), 219–232.
- Wang, D., Mori, J., 2011. Frequency-dependent energy radiation and fault coupling for the 2010 Mw 8.8 Maule, Chile, and 2011 Mw 9.0 Tohoku, Japan, earthquakes. *Geophys. Res. Lett.* 38 (22).
- Wellington, P., Brossier, R., Hamitou, O., Trinh, P., Virieux, J., 2017. Efficient anisotropic dip filtering via inverse correlation functions. *Geophysics* 82 (4), A31–A35. <https://doi.org/10.1190/geo2016-0552.1>.
- Wells, R.E., Blakely, R.J., Sugiyama, Y., Scholl, D.W., Dinterman, P.A., 2003. Basin-centered asperities in great subduction zone earthquakes: a link between slip, subsidence, and subduction erosion? *J. Geophys. Res., Solid Earth* 108 (B10).
- Ye, L., Lay, T., Kanamori, H., Rivera, L., 2016. Rupture characteristics of major and great (Mw  $\geq$  7.0) megathrust earthquakes from 1990 to 2015: 1. Source parameter scaling relationships. *J. Geophys. Res., Solid Earth* 121 (2), 826–844.